Cement & Concrete Composites 31 (2009) 379–387

Contents lists available at ScienceDirect

Cement & Concrete Composites

journal homepage: www.elsevier.com/locate/cemconcomp

Low velocity flexural impact behavior of AR glass fabric reinforced cement composites

Deju Zhu[a], Mustafa Gencoglu[b], Barzin Mobasher[a,*]

[a] Department of Civil and Environmental Engineering, Arizona State University, Tempe, AZ 85287, USA
[b] Division of Structural Engineering, Istanbul Technical University, Maslak, Istanbul 34469, Turkey

ARTICLE INFO

Article history:
Received 21 October 2008
Received in revised form 17 April 2009
Accepted 17 April 2009
Available online 3 May 2009

Keywords:
AR glass fabrics
Cement composite
Impact
Drop height
Pultrusion process

ABSTRACT

Fabric–cement composites developed using the pultrusion production process have demonstrated impressive tensile and flexural properties. For instance fabric reinforced composites with bonded Alkali Resistant (AR) glass fabrics exhibit strain-hardening behavior, tensile strength in the range of 20–25 MPa, and strain capacity of the order of 2–5% under static conditions. Properties of these composite systems were investigated under three point bending conditions using an instrumented drop weight impact system. Samples were studied from the viewpoint of the variations of impact load, deflection response, acceleration and absorbed energy. Development of the testing system in terms of components and acceleration response are discussed in detail. Methods of the impact load measurement using three different ways of acceleration response, piezoelectric load washer and conventional strain gage based load cell are discussed. Cement composites with two different fabric contents and four different drop heights of hammer (dropping mass) were tested. Experimental results indicate that for the same drop height, the stiffer beam type specimens have a lower ultimate deflection but a higher load carrying capacity than the plate type specimens. The maximum flexural stress and absorbed energy of composites increase with drop height. In beam specimens, complete fracture does not take place as cracks form and close due to rebound and significant microcracking in the form of radial fan cracking is observed, whereas interlaminar shear is the dominant failure mode in the plate specimens.

1. Introduction

Structural elements such as wall panels, hydraulic structures, airport pavements, military structures, and industrial floor overlays may be subjected to severe impact loads. Very high stress rates occur during such dynamic loads as a large amount of energy is transmitted to the structure in a short duration. Structural elements respond to earthquake and explosive forces by a variety of interactive mechanical properties. These properties include strength, absorbed energy, deformation capacity and ductility and must be present to maintain integrity without collapse. Fiber addition to concrete improves its ductility, tensile, impact, and flexural strength. Low-velocity impact on fiber-reinforced composites has been the subject of many experimental investigations [1–5]. Bindiganavile and Banthia [6,7] showed that the flexural strength of fiber reinforced concrete is higher under impact loading than under quasi-static loading. The energy absorption capacity is also higher under impact for concrete reinforced with polymeric fibers. Lok and Zhao [8] reported that the post-peak ductility of steel fiber reinforced concrete (SFRC) is lost at strain rates exceeding 50 s^{-1} since fragments can no longer bond onto the steel fibers. Choi and Lim [9] used a linearized contact law approach to address the impact response of composite laminates. Wang et al. [10] reported an increase in the fracture energy of the beams with an increasing volume of the hooked steel fibres in concrete mixture. Manolis et al. [11] showed that fibrillated polypropylene fibers significantly improved the impact resistance of concrete slabs. Li et al. [12] investigated static and impact behavior of extruded sheets with short fibers by using polyvinyl alcohol (PVA) and glass fibers. Results indicated that glass fibers were more effective in improving the tensile strength and impact properties, while PVA fibers increased the tensile strain and absorbed energy of specimens.

An efficient production method for fabric–cement composites is the pultrusion process. Cement composites containing 5% (AR) unidirectional glass fibers produced by pultrusion achieved tensile strength of 50 MPa [13]. A pultrusion based method to produce fabric–cement composite has been developed [14]. The behavior of fabric–cement composites exposed to tensile loads is characterized by multiple cracking. The nature of multiple cracking and the resulting stress–strain curve, toughness, and strength, are dependent on the properties of the reinforcing fabrics, the cement matrix, as well as the interface bond and the anchorage of the

---

* Corresponding author. Tel.: +1 480 965 0141; fax: +1 480 965 0557.
E-mail addresses: Deju.Zhu@asu.edu (D. Zhu), mgencoglu@ins.itu.edu.tr (M. Gencoglu), Barzin@asu.edu (B. Mobasher).

0958-9465/$ - see front matter © 2009 Elsevier Ltd. All rights reserved.
doi:10.1016/j.cemconcomp.2009.04.011

fabrics developed [15]. Microstructural features such as crack spacing, width, and density allow formulation of the damage evolution as a function of macroscopically applied strain [16,17].

In this study, the flexural impact behavior of Alkali Resistant (AR) Glass fabric reinforced cement composites made by pultrusion process was investigated in order to evaluate if the superior static response of these systems can be extended to the dynamic load cases as well. Composites with 6- and 8-layer of fabrics were tested in vertical and horizontal positions with respect to the direction of applied impact load. Four drop heights of 50 mm, 100 mm, 200 mm and 250 mm were used as the initial height of the drop hammer. The impact load was measured by three different methods, i.e. acceleration response of specimens, piezoelectric load cell and conventional strain gage based load cell. The time histories of impact loads, deflections, accelerations, the absorbed energy and the ratio of absorbed energy to input potential energy were discussed in detail.

2. Experimental program

2.1. Material properties and mix design

The bonded Alkali Resistant (AR) glass fabric consisted of a perpendicular set of yarns (warp and weft) glued together at the junction points and was coated with sizing during fabric production. The fabric had a density of 4 yarns per cm in both warp and weft directions, and was manufactured by NEG Glass, as shown in Fig. 1, using yarns of filament diameter of 13.5 μm, tensile strength of 1270–2450 MPa, and modulus of elasticity of 78 GPa. There are 400 filaments of fiber in a yarn resulting in a bundle diameter of 0.27 mm. The mix design of cement paste for the composites is presented in Table 1.

The pultrusion process was used to produce the fabric–cement based composite specimens [14]. In this approach, the fabrics were immersed in a slurry infiltration chamber, and then pulled through a set of rollers to squeeze the paste through the fabric openings. Composite laminates were formed on a rotating mandrel, as shown in Fig. 2. The cement based composites were made with six and eight layers of fabrics, resulting in reinforcement content of about 4.0% and 6.0% by volume of AR glass fibers, respectively. These are referred to as ARG6, and ARG8 composites. After curing, the panels were cut to dimensions of 50 × 150 mm, and eighteen specimens were obtained for each type of the composites. The thicknesses of ARG6, and ARG8 panels were around 7–9 mm and 11–13 mm, respectively.

2.2. Testing procedure

An impact test set-up based on a free-fall drop of an instrumented hammer on a three point bending specimen was developed. The schematic of the system is presented in Fig. 3. The drop heights range from 1 to 200 cm, and can be controlled by means of an electronic hoist and release mechanism. An anti-rebound system consisting of a pneumatic brake system triggered by a contact type switch was used to stop the hammer after the duration of impact was completed.

The experimental set-up consisted of several components described as follows. The entire moving part that impacts the specimen included the free weight, frictionless bearings along the drop columns, load cell, connection plate, and a set of threaded rods. This entire assembly was referred to as the hammer and weighed

Fig. 1. AR glass fabrics.

Table 1
Mix design of cement paste.

Material	Weight
Cement	8159 g
Water	3263 g
Silica fume	677 g
Superplasticiser	12 ml

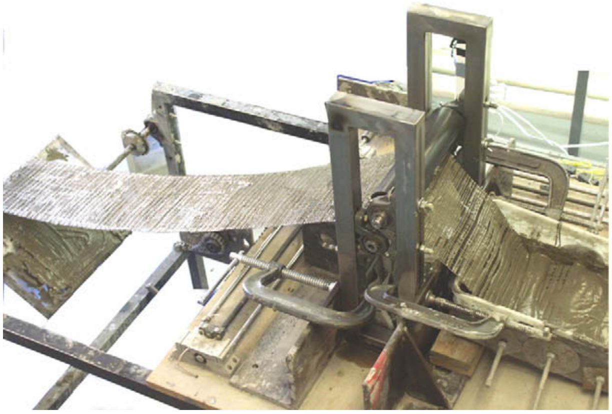

Fig. 2. Pultrusion process showing the fabrics pulled through the cement bath, pinch rollers and collecting on the flat rotating mandrel.

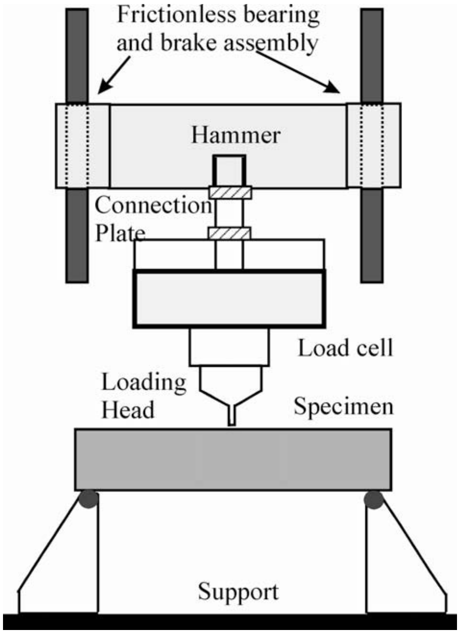

Fig. 3. Schematic diagram of the impact test set-up.

134 N. The hammer was released from a predetermined drop height by means of an electronic brake release mechanism. The impact force induced by the free fall weight was measured by different means including a load cell with a range of 90 kN mounted on the hammer behind the blunt shaped impact head. An alternative piezoelectric load washer, and also a set of accelerometers mounted on the specimen and hammer. A second strain gage based load cell with 90 kN capacity was mounted beneath the support plate and measured the force transmitted to the equipment base. A linear variable differential transformer (LVDT) with a range of ±10 mm was connected to the specimen by means of a lever arm. Three accelerometers were used to document the acceleration–time history of the hammer, specimen, and the support system. Two accelerometers with a capacity of ±500 g were mounted on the top load cell and tension zone of the specimen. The third accelerometer with the range of ±100 g was placed on bottom base of the equipment beneath the support plate. The data acquisition system consisted of a PC based National Instruments PCI acquisition card and LABVIEW VI's with trigger function which can record signals from load cell, accelerometers and the LVDT simultaneously at sampling rates of up to 100 kHz. The entire duration of the test lasted approximately 20 ms or less. Several MATLAB programs were developed for data processing to compute the frequency content of the specimen and equipment, filter and smooth the raw data with a low-pass filter, and calculate the mechanical properties.

The ARG6 and ARG8 specimens were tested in both vertical and horizontal positions with respect to the direction of applied impact load (beam and plate, respectively). The fabrics of composites in the vertical orientation (beam type) were parallel to the direction of load, referred to as ARG6B and ARG8B, while in the horizontal specimens the fabrics were perpendicular to the direction of load application (plate type), referred to as ARG6P and ARG8P. The span of composites was 127 mm for three-point flexural impact tests.

2.3. Dynamic calibration

The signal acquisition during a high dynamic test is strongly conditioned by the nature of the test procedures [18]. Rapid variation of the kinematical quantities excites vibrations depending on the stiffness and mass of the specimen, support, or the hammer, resulting in signal disturbances. Interpretation of raw signals without prior knowledge of the dynamic characteristics of the system would therefore be questionable. After the system dynamics are identified, it is essential to filter the data to retain the material responses [19].

Preliminarily experimental modal analysis tests were conducted to identify the predominant frequencies of the hammer and the test specimens. All the tests were conducted with sampling frequency of 20 kHz. Fig. 4a shows the Fourier amplitude spectra of the hammer by using Fast Fourier Transform (FFT) which shows the frequency content of the hammer acceleration data. The predominant frequency of the hammer is about 5 kHz. Using the same method, one can also get the predominant frequency of specimens which were less than 1 kHz and 2 kHz for ARG6P and ARG6B specimens, respectively as shown in Fig. 4b and c, respectively. Consequently, a low-pass filter with cutoff frequency of 2 kHz was selected to separate the high frequency response of the instrumentation from the test data. The filtered data was considered to represent the real response of the specimens. The Fourier amplitude

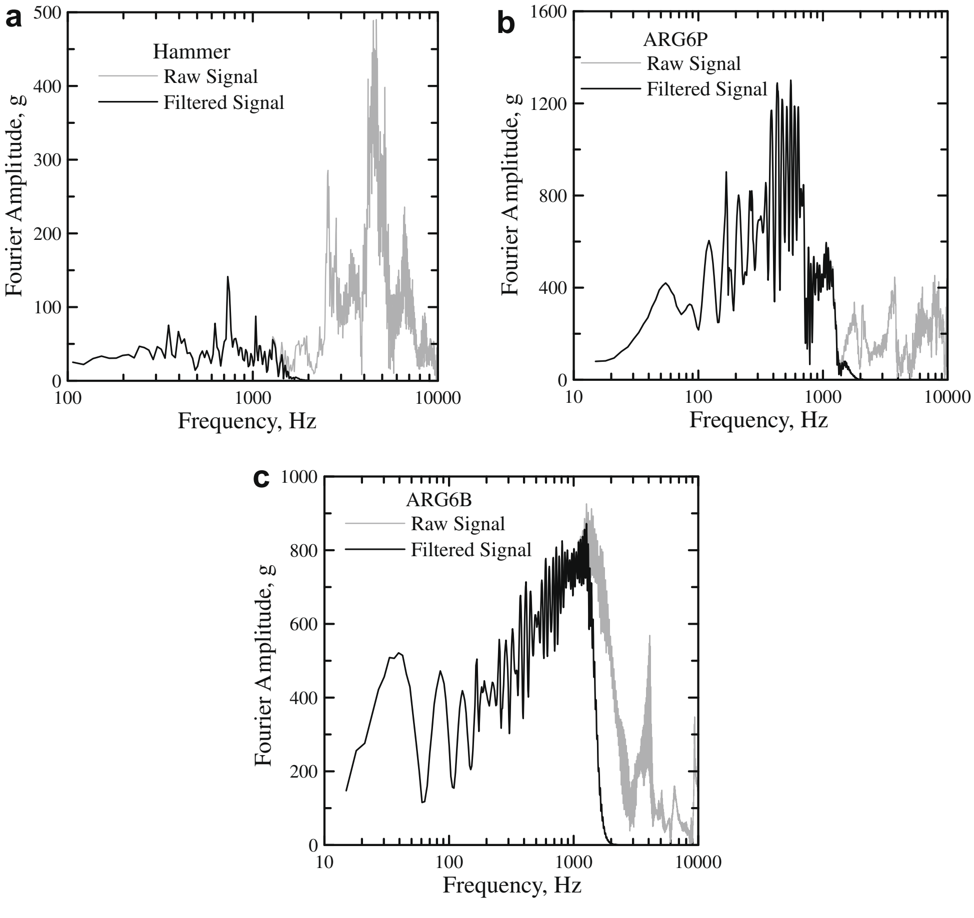

Fig. 4. Fourier amplitude spectrum of the acceleration of (a) hammer, (b) ARG6P specimen, and (c) ARG6B specimen.

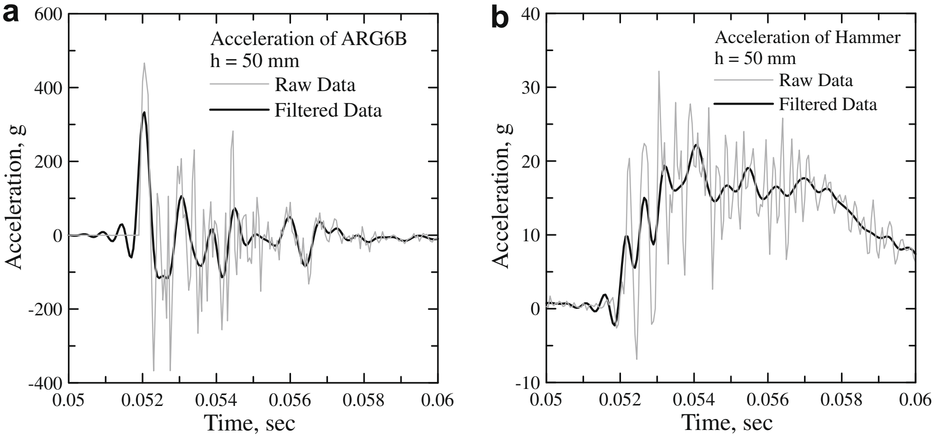

Fig. 5. Comparison of raw and filtered acceleration of (a) ARG6B specimen and (b) hammer.

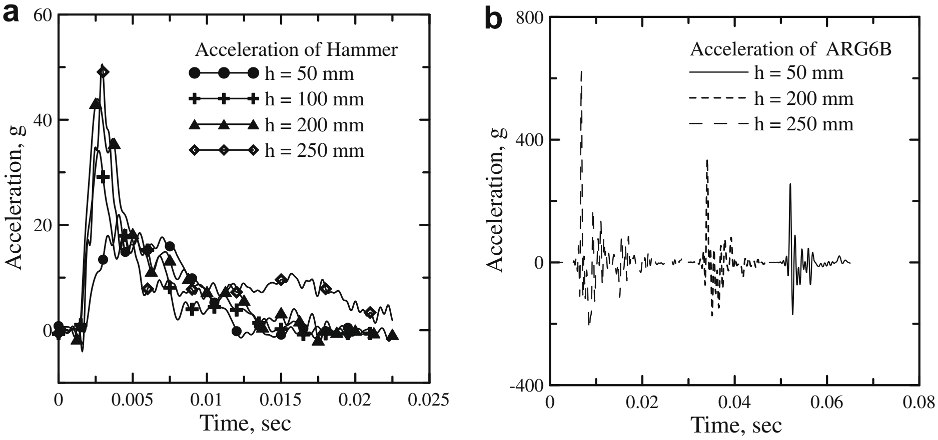

Fig. 6. Acceleration of (a) hammer and (b) ARG6B specimens at different drop heights.

spectra of filtered data were plotted in Fig. 4 as well. Fig. 5a and b indicates the difference between the original acceleration and filtered acceleration of the ARG6B specimen and hammer, respectively. As the high frequency contents are filtered out, acceleration amplitudes much lower than original values are obtained.

The acceleration–time history of hammer and specimen were recorded by two individual accelerometers. As shown in Fig. 6a, the acceleration of hammer at four different drop heights of 50 mm, 100 mm, 200 mm, and 250 mm, indicates that the peak acceleration during impact is increasing with drop height from about 20 g at drop height of 50 mm to 50 g at drop height of 250 mm. Fig. 6b shows the acceleration of ARG6B specimens during impact at three different drop heights of 50, 100, and 200 mm. The transient peak specimen acceleration experienced increases from 270 g at drop height of 50 mm to 610 g at drop height of 250 mm. Since the mass of specimen is around 0.2 kg, according to Newton's second law of motion, an inertial force of 54 N is obtained at drop height of 50 mm. This value is roughly 3% of the impact force measured by the conventional load cell. At higher impact heights such as 250 mm, the inertial force is about 120 N which is still about 3% of the impact force measured by the conventional load cell. The inertial force on the specimen during impact was therefore neglected.

The procedure to obtain impact force from hammer acceleration data was used as a verification check. The force history was calculated by applying the Newton's second law to measured acceleration data:

$$F(t) = m \times a(t) \tag{1}$$

where $a(t)$ is the acceleration history and m is the mass of the hammer.

Fig. 7a and b shows the force response measured by the conventional load cell and calculated from acceleration of the hammer according to Eq. (1), respectively. The acceleration was filtered by a low-pass filter as discussed previously. There is negligible difference between the calculated impact force with that measured by the conventional load cell at drop height of 50 mm. However, at the drop heights of 100 mm and above, the calculated impact force dramatically increases as compared to the conventional load cell measurement. For example at drop height of 200 mm, the impact force measured by the conventional load cell is 4000 N, while the calculated impact force is 6000 N.

In order to evaluate the accuracy of force measurement of the conventional load cell, a Kistler 9041A piezoelectric load washer with a capacity of 90 kN and rigidity of 7.5 kN/μm was installed between the conventional load cell and blunt shaped impact head. The response frequency of the load washer is 33 kHz. The load signal was amplified through a Kistler 5010B dual mode charge amplifier. The signals were filtered by a low-pass filter with cut-off frequency of 2 kHz to eliminate high frequency noise during

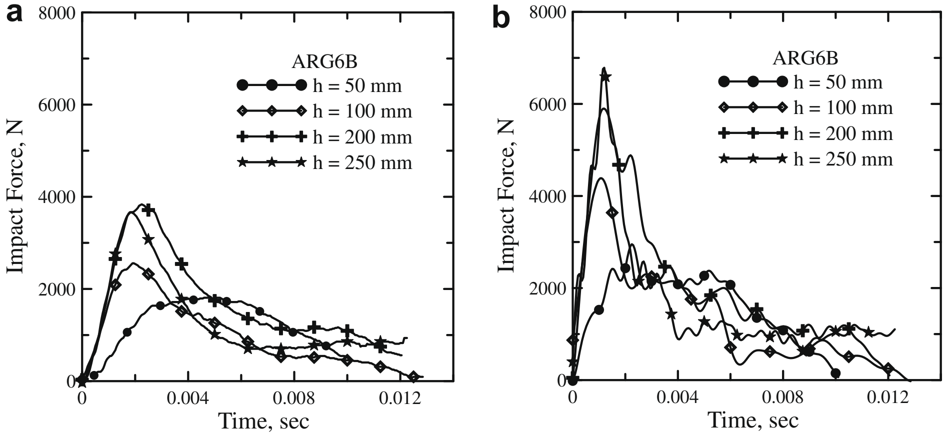

Fig. 7. Impact force variation for ARG6B specimens at different drop heights: (a) measured by conventional load cell and (b) calculated from acceleration of hammer (according to Eq. (1)).

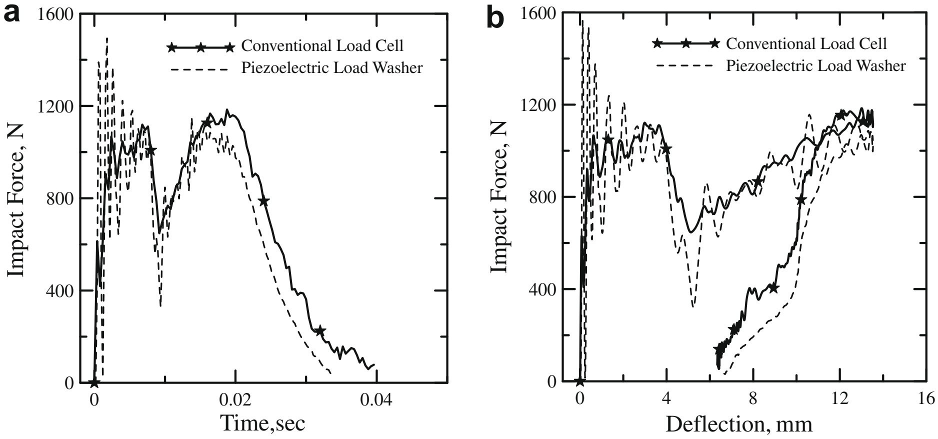

Fig. 8. Comparison of impact forces measured by conventional load cell and piezoelectric load washer: (a) impact force vs. time and (b) impact force vs. deflection.

data processing. Fig. 8a and b shows the comparison of impact force measured by the conventional load cell and the piezoelectric load washer vs. time and deflection, respectively. The impact force measured by the piezoelectric load washer has more oscillations than the conventional load cell during the initial loading range. This behavior is due to the specimen and the hammer reacting to the impact by oscillating at their natural frequencies, while the piezoelectric load washer has a higher response frequency than the conventional load cell and is able to acquire details of the oscillation. In consideration to the absorbed energy, there is negligible difference between them based on the impact force measured by these two load transducers. Therefore, results listed are based on the impact force measured by the conventional load cell.

The input energy is the potential energy of the hammer and depends on its drop height, mass and the amount of energy lost during the free fall drop of the hammer. Some of the input energy is absorbed by the test specimen, while the remaining energy is either dissipated by friction, or transferred to the test set-up through the supports after the impact event.

The input potential energy of the hammer, $U_{i,}$ was defined as follows:

$$U_i = mgH = \frac{1}{2}mv_0^2 + U_d = U_k + U_f + U_d \qquad (2)$$

where m is same as above, g is the acceleration of gravity, H is the drop height of hammer, v_0 represents the hammer velocity prior to impact, U_d represents the frictional dissipated energy between the time of release of the hammer until just prior to the impact event, U_k represents the absorbed energy by the specimen, and U_f represents the energy remaining in the system after the failure of the specimen has taken place. This energy may be elastically stored in the sample, and result in the rebound, or transmitted through the specimen to the support.

The absorbed energy (kinetic energy dissipated in the specimen), U_k, was defined as follows:

$$U_k = \int_{t=0}^{t=t^*} P(t)v(t)dt \approx \sum P(t)\Delta d(t) \qquad (3)$$

where $P(t)$ and $v(t)$ represent the force and velocity history of the impact event, t^* represents the impact event duration, $\Delta d(t)$ represents the deflection increment history of test specimen.

The maximum flexural stress, σ_f, was measured using the linear elastic small displacement bending equation as follows:

$$\sigma_f = \frac{3}{2}\frac{P_m L}{bh^2} \qquad (4)$$

where P_m is the maximum load recorded during testing, b and h are the width and thickness of the test specimen, respectively, L is the specimen span.

Fig. 9 represents the time history of impact load, deflection, and acceleration response of a test specimen subjected to low-velocity impact from a drop height of 100 mm. Note that both the acceler-

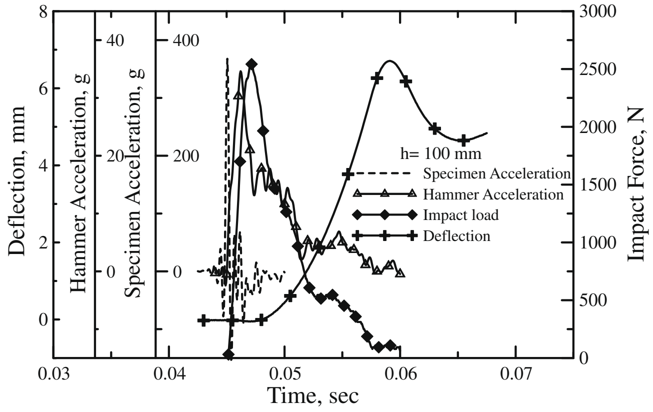

Fig. 9. Time history of load, deflection, and acceleration of composite specimen subjected to low-velocity impact.

ation and deceleration response of the hammer and the specimen indicate that the specimen may accelerate after the initial contact to as high as 330 g, and experience loads of up to 2600 N. There is a phase lag in the deflection signal due to the loading of the specimen as the maximum deflection is achieved while the load drops significantly; the specimen decelerates and comes to rest as the load and deflection signals stabilize after the impact event. Permanent deflection and post failure oscillations exist after the impact event.

3. Discussion of test results

3.1. Effect of drop height

The ARG6B specimens were tested at hammer drop heights of 50, 100, 200 and 250 mm and the input energy varied from 7 to 35 J. Fig. 10a shows the impact load–deflection curves of the ARG6B specimens tested for all the drop heights. At drop heights of 50, 100, and 200 mm, the rebound of specimens after impact is evident. In this case, it is shown that the ARG6B specimen respond to the impact loads as a stiff beam. The area under the impact load–deflection curve is the deformation energy that is initially progressively transferred from the hammer to the beam and then given back from the beam to the rebounding hammer, the area included inside the curve refers to the energy absorbed by the test specimen during impact [20]. At drop height of 250 mm, the impact load–deflection curve after peak force was flat, indicating no rebound. The area under the curve is the deformation energy that is progressively transferred from the hammer to the specimen, in this case of absence of rebound, is also the energy absorbed during the impact [20].

The ARG8B specimens were tested at hammer drop heights of 50, 100, and 200 mm and the input energy varied from 7 to 28 J. Fig. 10b shows the impact force vs. deflection curves, indicating that the impact forces increase proportional to the hammer drop height increased of up 100 mm. For the drop height of 200 mm, the ARG8B specimens were slightly stronger than those tested at 100 mm. It also shows that negative deflection (specimen rebound), as much as 1–2 mm, was present at mid-span of specimen at the drop height of 200 mm. Since the lever part of the deflection measurement system was connected at the mid-span, the LVDT measured the deflection as well as the rebound of specimen. The rebound of the ARG8B specimens could not be prevented by pneumatic brake system. Their absorbed energy gradually increased up to the drop height of 100 mm as calculated to the point of rebound. Due to rebound, the maximum deflection and absorbed energy of test specimen at the drop height of 200 mm was not compared with those at other drop heights.

Table 2 summarizes the impact response of all test specimens. For the ARG6B specimens, the impact force increased as the drop height increased initially, and remained almost constant at drop heights of 200 and 250 mm. The absorbed energy also increased with the drop height. While for ARG8B specimens, the impact force increased from 2076 N at the drop height of 50 mm to 3618 N at the drop height of 100 mm, however there were no significant increases at the drop height of 200 mm. The absorbed energy continuously increased as the hammer drop height increased. It was also observed that the deflections of ARG6B and ARG8B specimens continuously increased as the drop height increased.

The ARG6P and ARG8P specimens which represented a plate loading condition were tested at drop heights of 50 and 100 mm. Higher drop heights were not attempted since the specimen failed due to inter-laminar shear. The impact load, maximum flexural stress, absorbed energy, and maximum deflection of ARG6P specimens increased from 799 to 1062 N, from 17.8 to 29.9 MPa, from 4.03 to 5.04 J, and from 9.23 to 14.67 mm, respectively when the drop height increased from 50 to 100 mm. The impact load, maximum flexural stress, absorbed energy, and maximum deflection of ARG8P specimens increased from 585 to 934 N, from 12.45 to 27.5 MPa, from 2.57 to 4.89 J, and from 5.58 to 10.21 mm, respectively when the drop height increased from 50 to 100 mm.

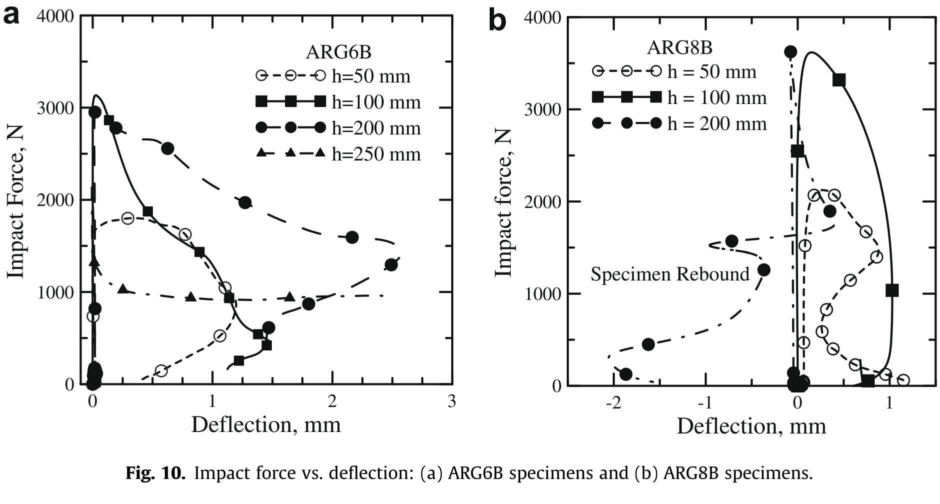

Fig. 10. Impact force vs. deflection: (a) ARG6B specimens and (b) ARG8B specimens.

Table 2
Summary of impact response of AR glass composite specimens.

Specimen type	Drop height (mm)	Potential energy (J)	Drop velocity (m/s)	Max. impact force (N)	Max. stress (MPa)	Max. deflection (mm)	Absorbed energy (J)
ARG6P	50	7	1.0	799	17.8	9.23	4.03
	100	14	1.4	1062	29.9	14.67	5.04
ARG6B	50	7	1.0	1802	10.5	1.24	1.68
	100	14	1.4	2501	16.6	1.63	2.29
	200	28	2.0	3771	24.8	2.58	3.93
	250	35	2.2	3569	23.2	3.32	4.90
ARG8P	50	7	1.0	585	12.45	5.58	2.57
	100	14	1.4	934	27.5	10.21	4.89
ARG8B	50	7	1.0	2076	14.3	0.97	2.78
	100	14	1.4	3618	19.7	1.63	2.96
	200	28	2.0	3638	22.0	3.58	3.42

3.2. Effect of number of lamina and specimen orientation

It is observed that the maximum flexural stress and absorbed energy of beam specimens increased with the number of fabric layers, while in the plate specimens, the same properties decreased with an increase in the number of fabric. The failure in the plate specimens was due to inter-laminar shear failure. At the drop height of 50 mm, the maximum impact force of ARG8B specimens was about 15% higher than the ARG6B composites as shown in Table 2. Due to the higher specimen stiffness in the beam mode compared to the plate mode, beam specimens had lower deflections during impact than plate specimens. At the same drop height, the impact force experienced by beam specimens was much higher than plate specimens regardless of means of force measurement by the conventional load cell or acceleration response of the hammer as shown in Fig. 11. For ARG6P specimens at the drop height of 50 mm, the maximum impact force measured by the conventional load cell was slightly less than the calculated force. However, ARG6B specimen showed that the maximum impact force was about 1800 N measured by load cell and was about 2300 N for averaged computed value of multiple peaks. Fig. 11 also shows that the test duration of ARG6B specimen is only half of that of ARG6P specimen. In beam specimens, complete fracture does not take place as cracks form and close due to rebound, whereas in plate specimens, interlaminar shear is the dominant failure mode. The beam specimens utilize the fabrics as shear reinforcement as well as flexural reinforcement, whereas in the plate samples the role of fabric is primarily in the flexural reinforcement and there is no resistance offered to shear delamination.

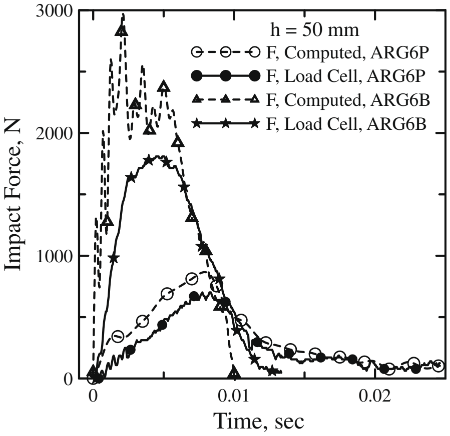

Fig. 11. Effect of specimen orientation, impact forces measured by conventional load cell and calculated from acceleration of hammer according to Eq. (1).

3.3. Crack pattern

Typical patterns of distributed cracks forming in composites were investigated after impact. The crack propagation and failure mode of composites were similar to each other for ARG6 and ARG8 specimens. The response however was different for beam and plate samples as shown in Fig. 12a and b, respectively. Significant microcracking in the form of radial fan cracking is observed in the beam specimen. As flexural cracks occur, the fabric reinforce-

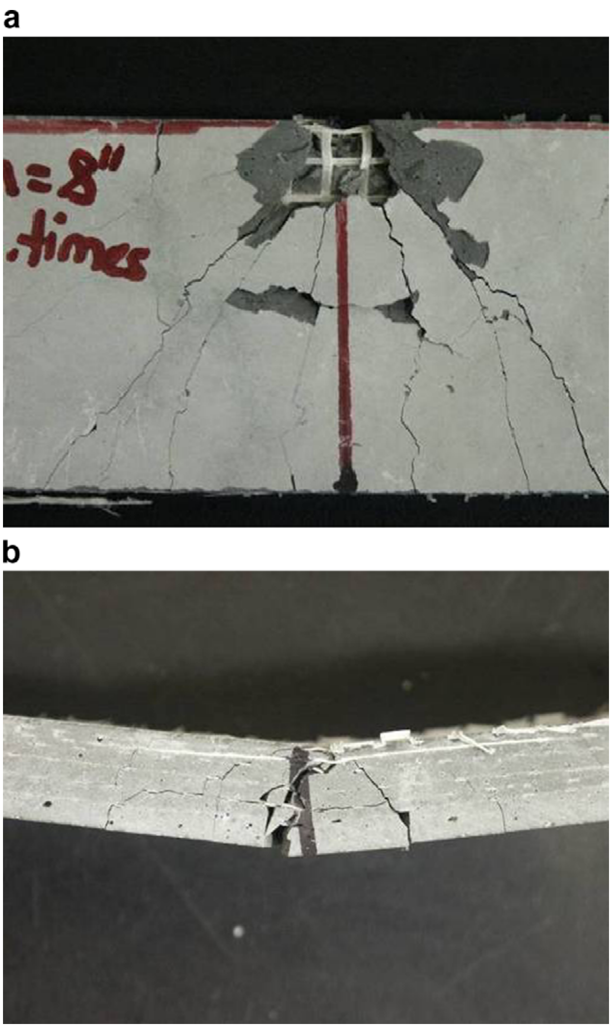

Fig. 12. The views of damages on the cement based composites after impact for the drop height of 200 mm: (a) beam specimen and (b) plate specimen.

ment provides bridging across the newly formed cracks and promotes additional cracking away from the centerline. A parallel set of fan cracks form along the span of the specimen. The compression failure at the point of impact also causes degradation, however, the main pattern observed is the distributed cracking in the tensile zone. This pattern can be characterized by the a well defined set of cracks with regular spacing that are formed in the tensile zone, however as one moves up the beam section, these cracks converge to the point of impact. Distributed cracking is also observed in the plate specimens. The cracks of the beam specimens at the drop height of 200 mm were wider and longer than those at drop height of 100 mm, and were diagonally extended from the impact point to both support points. The damage of the specimen at drop height of 100 mm remained localized around the impact point. The crack propagation in beam specimens at drop height of 200 mm is similar to the response of deep beams in flexure with sufficient shear reinforcement.

In the plate specimen the extent of cracking is dominated by matrix flexural cracks which ultimately redirect and convert to interlaminar shear cracks. A bending matrix crack located at the surface ply generates a delamination along the first interface of the cracked ply. Matrix cracks within each lamina are arrested by the yarns of the fabric which effectively bridge them, allowing for additional cracks to form. These matrix cracks propagate into the nearby interface and cause the delamination between two plies. Intra-ply matrix cracks due to transverse shear initiate the main damage. Shear matrix cracks located in the inner plies of the laminate can generate a substantial delamination since crack propagation in-between plies is unopposed.

3.4. Energy absorption

The input potential energy was determined as a function of the hammer drop height and weight, assuming that no frictional losses took place during the free fall. Eq. (2) can be simplified as follows:

$$U_i = mgH = \frac{1}{2} m v_0^2 = U_k + U_f \tag{5}$$

The ratio of the absorbed energy to the input potential energy was determined for each drop height, defined as follows:

$$\beta = \frac{U_k}{U_i} \tag{6}$$

The absorbed energy and its ratio to the input energy were determined for each drop height for ARG6B and ARG8B specimens, as shown in Fig. 13. The absorbed energy increased with drop height while the ratio of absorbed energy to potential energy decreased with drop height for ARG6B specimens. The absorbed energy and the ratio of absorbed energy to potential energy for ARG8B specimens have similar trends. They increased first and then decreased when the drop height increased from 50 mm to 100 mm, and then to 200 mm. Although ARG8B specimens carried higher impact loads than ARG6B specimens, their absorbed energy levels are comparatively lower for the same drop height levels. This behavior can be attributed to ARG8B specimens displaying less deflection than ARG6B specimens due to stiffer behavior, allowing less damage to take place.

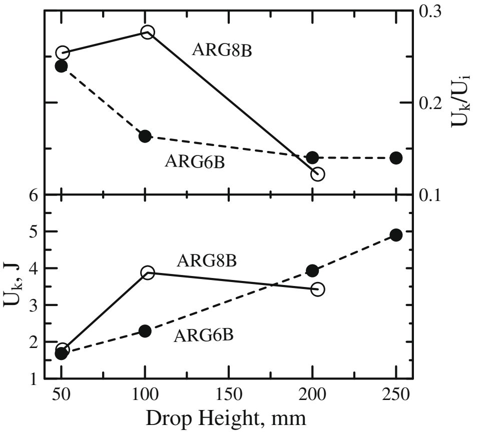

Fig. 13. Effect of fabric layer numbers and drop heights on the absorbed energy and ratio of absorbed energy to the input potential energy for beam specimens.

4. Conclusions

The flexural impact behavior of Alkali Resistant (AR) glass fabric composites subjected to low-velocity impact loading was studied. The experimental set-up allows acquisition of the impact force, accelerations of hammer and test specimen, and the deflection at mid-span of composite specimens. The acceleration data of hammer and specimen provide alternative methods to calculate the impact force experienced by specimen and study the inertial effect during impact loading. The system dynamics were identified and a low-pass filter with cut-off frequency of 2 kHz was effectively used to eliminate the noise due to oscillation of equipment and specimen at their natural frequencies. Test results were evaluated to determine the flexural impact behavior in terms of maximum flexural stress, maximum deflection, absorbed energy, and crack patterns of the specimens. The results can be summarized as the follows:

(1) Beam type specimens had a larger load carrying capacity with a lower deflection than plate specimen due to coupled effect of the orientation of cross-section and the direction of fabric.
(2) The maximum flexural stress and absorbed energy of beam specimens increased with the number of fabric layers. The maximum flexural stress and absorbed energy of plate specimens decreased with the number of fabric layers due to inter-laminar shear failure. Maximum flexural stress as high as 29.9 MPa for plate specimens was observed when subjected to a range of potential energy in the range of 7–14 J, and as high as 24.8 MPa for beam specimens when the potential energy was in the range of 7–35 J.
(3) The total absorbed energy increased with drop height while the ratio of absorbed energy to potential energy decreased with drop height for ARG6B specimens. In the ARG8B specimens, the absorbed energy and the ratio of absorbed energy to potential energy have similar trends. They increased first and then decreased when the drop height increased from 50 mm to 100 mm, and then to 200 mm.
(4) In the beam specimens, complete fracture does not take place as cracks form and close, whereas in the plate specimens, interlaminar shear is the dominant failure mode. Localized compression failure at the point of impact causes degradation, however, the main pattern observed is the distributed cracking in the tensile zone.

Acknowledgements

The authors acknowledge the support of National Science Foundation, program 0710807, Dr. Osman Shinaishin, Program Officer for support of this project. Dr. Dallas Kingsbury and Mr. Peter Goguen, helped with instrumentation, and Mr. John Jones of NEG America for contributed the fabrics materials. Financial support of NCF, the Foundation of Istanbul Technical University for Dr. Gencoglu is greatly appreciated.

References

[1] Liu D, Raju BB, Dang X. Size effects on impact response of composite laminates. Int J Impact Eng 1998;21(10):837–54.

[2] Tang TT, Saadatmanesh HPE. Behavior of concrete beams strengthened with fiber-reinforced polymer laminates under impact loading. J Compos Constr 2003;7(3):209–18.

[3] Bindiganavile V, Banthia N, Aarup B. Impact response of ultra-high strength fiber reinforced cement composite. ACI Mater J 2002;99(6):543–8.

[4] Alhozaimy AM, Soroushian P, Mirza F. Mechanical properties of polypropylene fiber reinforced concrete and the effects of pozzolanic materials. Cem Concr Compos 1996;18:85–92.

[5] Banthia N, Yan C, Sakai K. Impact resistance of fiber reinforced concrete at subnormal temperatures. Cem Concr Compos 1998;20:393–404.

[6] Bindiganavile V, Banthia N. Polymer and steel fiber-reinforced cementitious composites under impact loading, part 1: bond–slip response. ACI Mater J 2001;98(1):10–6.

[7] Bindiganavile V, Banthia N. Polymer and steel fiber-reinforced cementitious composites under impact loading, part 2: flexural toughness. ACI Mater J 2001;98(1):17–24.

[8] Lok TS, Zhao PJ. Impact response of steel fiber-reinforced concrete using a split Hopkinson pressure bar. J Mater Civil Eng 2004;16(1):54–9.

[9] Choi IH, Lim CH. Low-velocity impact analysis of composite laminates using linearized contact law. Compos Struct 2004;66:125–32.

[10] Wang NZ, Sidney M, Keith K. Fiber reinforced concrete beams under impact loading. Cem Concr Res 1996;26(3):363–76.

[11] Manolis GD, Gareis PJ, Tsono AD, Neal JA. Dynamic properties of polypropylene fiber-reinforced concrete slabs. Cem Concr Compos 1997;19:341–9.

[12] Li Z, Mu B, Chui SNC. Static and dynamic behavior of extruded sheets with short fibers. J Mater Civil Eng 2001;13(4):248–54.

[13] Mobasher B, Pivacek A, Haupt GJ. Cement based cross-ply laminates. J Adv Cem Based Mater 1997;6:144–52.

[14] Peled A, Mobasher B. Pultruded fabric–cement composites. ACI Mater J 2004;102(1):15–23.

[15] Peled A, Sueki S, Mobasher B. Bonding in fabric–cement systems: effects of fabrication methods. Cem Concr Res 2006;36(9):1661–71.

[16] Mobasher B, Peled A, Pahilajani J. Distributed cracking and stiffness degradation in fabric–cement composites. Mater Struct 2006;39(3):17–331.

[17] Peled A, Mobasher B. Properties of fabric–cement composites made by pultrusion. Mater Struct 2006;39(8):787–97.

[18] Cheresh MC, McMichael S. Instrumented impact test data interpretation. In: Kessler SL, et al., editors. Instrumented impact testing of plastic and composite materials. ASTM STP 963, Philadelphia; 1987.

[19] Cain PJ. Digital filtering of impact data. In: Kessler SL, et al., editors. Instrumented impact testing of plastic and composite materials. ASTM STP 963, Philadelphia; 1987.

[20] Belingardi G, Vadori R. Low velocity impact tests of laminate glass–fiber–epoxy matrix composite material plates. Int J Impact Eng 2002;27:213–29.